Sarnen - Kantonsschule (SARK)

SITE CHARACTERIZATION REPORT

Clotaire MICHEL, Stefano MARANÒ, Valerio POGGI

Jan BURJANEK, Daniel ROTEN, Carlo CAUZZI, Donat FÄH
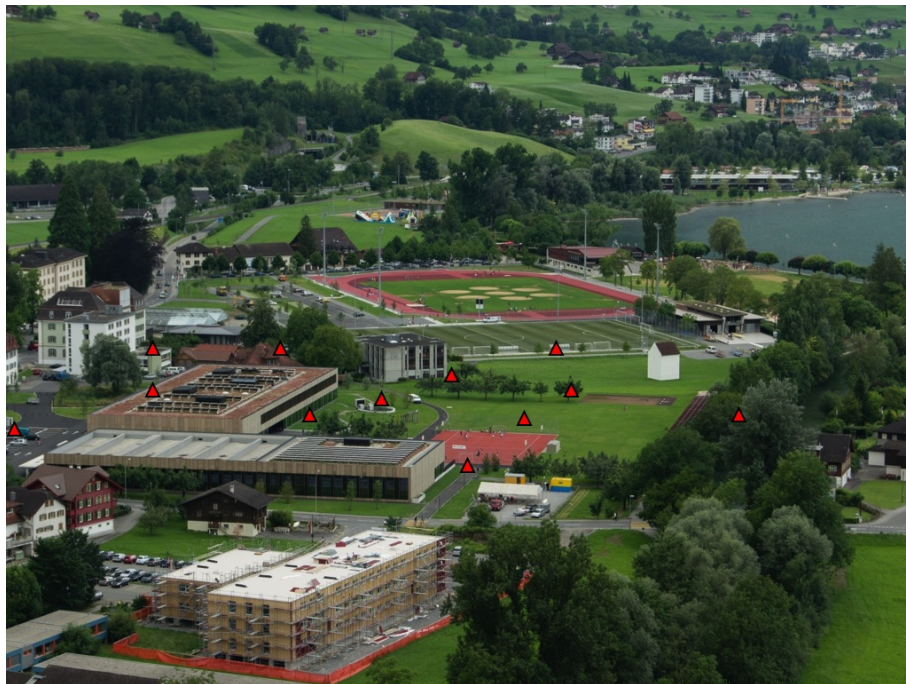
Sonneggstrasse 5 CH-8092 Zürich Switzerland; E-mail: clotaire.michel@sed.ethz.ch

Last modified : November 5, 2013

1

2

Abstract

Ambient vibration array measurements were performed to characterize the lacustrine deposits at site Sarnen Kantonsschule. The new station SARK of the Swiss Strong Motion Network, installed at this site, replaces the dial-up station SARG. In order to characterize the velocity profile under the station, array measurements with a $200\,\text{m}$ aperture were performed. The measurements were successful and allowed deriving a velocity model for this site. The soil column underlying station SARK is made of a $8 - 10\,\text{m}$ sedimentary layer with $V_s = 270\,\text{m/s}$ on more consolidated sediments with a velocity larger than $V_s = 800\,\text{m/s}$. The velocity reaches $1400\,\text{m/s}$ at $40\,\text{m}$ and is stable down to the bedrock, found around $160\,\text{m}$ with a large uncertainty. This velocity contrast produces a fundamental resonance peak at $2.3\,\text{Hz}$. Contrarily to what was expected, the loose infill sediments of this basin are therefore very shallow and most of the basin is filled with stiff sediments. $V_{s,30}$ is found to be close to $540\,\text{m/s}$. This configuration corresponds to ground type E for EC8 [CEN, 2004] and SIA261 [SIA, 2003]. The theoretical elastic SH transfer function and the impedance contrast of the quarter-wavelength velocity computed from the inverted profiles show large amplifications at $6 - 8\,\text{Hz}$ due to the weak upper layer. Recordings of the new station will allow to validate these simple 1D models.

Contents

1   Introduction

The station SARK (Sarnen - Kantonsschule) is part of the Swiss Strong Motion Network (SSM-Net) in Central Switzerland. SARK has been installed in the framework of the SSMNet Renewal project in 2012 to replace the dial-up station SARG, located as well in the Sarnen basin, but further North-East. This project includes also the site characterization. The passive array measurements have been selected as a standard tool to investigate these sites. Such a measurement campaign was carried out on 12th July 2012 around the Kantonsschule (Fig. 1), with a centre at station SARK, in order to characterize the sediments under this station. The city of Sarnen suffered damage in 1964 due to a sequence of M 5 earthquakes. According to the geological map, this station is located on loose glacial-lacustrine sediments in the plain between lake Sarnen and lake Lucerne. This report presents the measurement setup, the results of the H/V analysis and of the array processing of the surface waves (dispersion curves). Then, an inversion of these results into velocity profiles is performed. Standard parameters are derived to evaluate the amplification at this site.

Canton	City	Location	Station code	Site type	Slope
Obwald	Sarnen	Kantonsschule	SARK	Lacustrine plain	Flat

Table 1: Main characteristics of the study-site.

Figure 1: Picture of the site with location of the array stations of the second dataset (red triangles).

2 Experiment description

2.1 Ambient Vibrations

The ground surface is permanently subjected to ambient vibrations due to:

- natural sources (ocean and large-scale atmospheric phenomena) below $1\,\text{Hz}$,

- local meteorological conditions (wind and rain) at frequencies around $1\,\text{Hz}$,

- human activities (industrial machines, traffic...) at frequencies above $1\,\text{Hz}$ [Bonnefoy-Claudet et al., 2006].

The objective of the measurements is to record these ambient vibrations and to use their propagation properties to infer the underground structure. First, the polarization of the recorded waves (H/V ratio) is used to derive the resonance frequencies of the soil column. Second, the arrival time delays at many different stations are used to derive the velocity of surface waves at different frequencies (dispersion). The information (H/V, dispersion curves) is then used to derive the properties of the soil column using an inversion process.

2.2 Equipment

For these measurements 12 Quanterra Q330 dataloggers named NR01 to NR12 and 14 Lennartz 3C 5 s seismometers were available (see Tab. 2). Each datalogger can record on 2 ports A (channels EH1, EH2, EH3 for Z, N, E directions) and B (channels EH4, EH5, EH6 for Z, N, E directions). Time synchronization was ensured by GPS. The sensors were placed on a metal tripod in a $20\,\text{cm}$ deep hole, when possible, for better coupling with the ground.

Digitizer	Model	Number	Resolution
	Quanterra Q330	12	24 bits
Sensor type	**Model**	**Number**	**Cut-off frequency**
Velocimeter	Lennartz 3C	14	0.2 Hz

Table 2: Equipment used.

2.3 Geometry of the arrays

Two array configurations were used, for a total of 4 rings of 15, 25, 50 and $100\,\text{m}$ radius around a central station. The first configuration includes the 3 inner rings with 14 sensors; the second configuration includes the 2 outer rings (plus 1 of the first ring and an additional station in the ring 3) with 13 sensors. The minimum inter-station distance and the aperture are therefore 15 and $100\,\text{m}$ and 15 and $200\,\text{m}$, respectively. The experimental setup is displayed in Fig. 2. The final usable datasets are detailed in section 3.2.
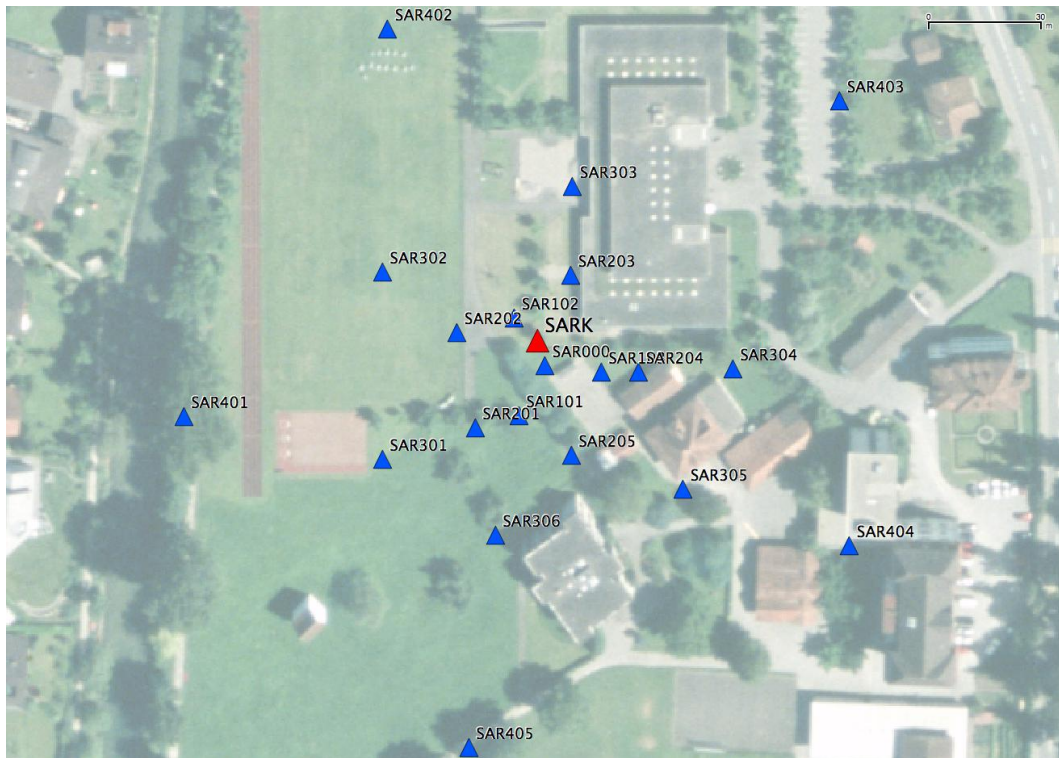
Figure 2: Geometry of the arrays.

2.4   Positioning of the stations

The sensor coordinates were measured using a differential GPS device (Leica Viva GS10), including only a rover station and using the Real Time Kinematic technique provided by Swisstopo. It allowed an absolute positioning with an accuracy better than $5\,\mathrm{cm}$ on the Swissgrid except for point SAR303 with a precision of $25\,\mathrm{cm}$, due to the close building disturbing the signal. This precision was assumed sufficient for this processing.

3 Data quality

3.1 Usable data

The largest time windows were extracted, for which all the sensors of the array were correctly placed and the GPS synchronization was ensured. The array was limited in size by the river and main roads, where the traffic was limited. A light wind was blowing during the measurements. GPS positioning measurements were mostly not performed during the recordings to avoid additional noise. Children started to play football between rings 3 and 4 at 11:00 UTC (end of dataset 1) on a damped field. It seems it did not dramatically affect the recordings.

Orientation of the sensor was checked by maximizing the correlation with the central station at low frequencies [Poggi et al., 2012b]. Deviations lower than $10\,^\circ$ were found for all points. Original and rotated datasets are available for the 3C array analysis.

The spectra show that points SAR101 and SAR302 have a higher noise level in all components at low and intermediate frequencies, which can be due to bad coupling. An undamped peak can be seen at $2.77\,\mathrm{Hz}$ in the vertical direction for all recordings of the first dataset. Finally, point SAR401 has particularly high noise amplitude due to either the river or the pedestrian pathway.

The characteristics of the datasets are detailed in Tab. 3.

3.2 Data processing

The data were first converted to SAC format including in the header the coordinates of the point (CH1903 system), the recording component and a name related to the position. The name is made of 3 letters characterizing the location (SAR here), 1 digit for the ring and 2 more digits for the number in the ring. Recordings were not corrected for instrumental response.

Dataset	Starting Date	Time	Length	F_s	Min. inter-distance	Aperture	# of points
1	2012/07/12	9:24	120 min	200 Hz	15 m	100 m	14
2	2012/07/12	11:56	122 min	200 Hz	15 m	200 m	13

Table 3: Usable datasets.

4   H/V processing

4.1   Processing method and parameters

In order to process the H/V spectral ratios, several codes and methods were used. The classical H/V method was applied using the Geopsy `http://www.geopsy.org` software. In this method, the ratio of the smoothed Fourier Transform of selected time windows are averaged. Tukey windows (cosine taper of 5% width) of $50\,\mathrm{s}$ long overlapping by 50% were selected. Konno and Ohmachi [1998] smoothing procedure was used with a b value of 80. The classical method computed using the method of Fäh et al. [2001] was also performed.

Moreover, the time-frequency analysis method [Fäh et al., 2009] was used to estimate the ellipticity function more accurately using the Matlab code of V. Poggi. In this method, the time-frequency analysis using the Wavelet transform is computed for each component. For each frequency, the maxima over time (10 per minute with at least $0.1\,\mathrm{s}$ between each) in the TFA are determined. The Horizontal to Vertical ratio of amplitudes for each maximum is then computed and statistical properties for each frequency are derived. A Cosine wavelet with parameter 9 is used. The mean of the distribution for each frequency is stored. For the sake of comparison, the time-frequency analysis of Fäh et al. [2001], based on the spectrogram, was also used, as well as the wavelet-based TFA coded in Geopsy.

The ellipticity extraction using the Capon analysis [Poggi and Fäh, 2010] as well as fundamental mode obtained using the wavefield decomposition method [Maranò et al., 2012] (see section on array analysis) were also performed.

Method	Freq. band	Win. length	Anti-trig.	Overlap	Smoothing
Standard H/V Geopsy	$0.2 - 20\,\mathrm{Hz}$	$50\,\mathrm{s}$	No	50%	K&O 80
Standard H/V D. Fäh	$0.2 - 20\,\mathrm{Hz}$	$30\,\mathrm{s}$	No	75%	-
H/V TFA Geopsy	$0.2 - 20\,\mathrm{Hz}$	Morlet m=8 fi=1	No	-	-
H/V TFA D. Fäh	$0.2 - 20\,\mathrm{Hz}$	Specgram	No	-	-
H/V TFA V. Poggi	$0.2 - 20\,\mathrm{Hz}$	Cosine wpar=9	No	-	No

Table 4: Methods and parameters used for the H/V processing.

4.2   Results

Test station XSAR1 recorded continuously at the centre of the array during a week. Classical H/V from this long term recording is displayed on Fig. 3. It shows a fundamental frequency with low amplitude at $2.28\,\mathrm{Hz}$ and a second peak at $6.3\,\mathrm{Hz}$.

Looking at the array data, all H/V curves (Fig. 4) show a bump with a peak frequency around $0.6 - 0.7\,\mathrm{Hz}$ that is most probably related to the wind that was blowing during the measurement (direct action on the sensors, not ground vibrations) since it could not be seen on the long term recording. Moreover, the amplitudes at these frequencies are much different indicating it is not related to ground vibrations, but to disturbances of the sensors. Data below $2\,\mathrm{Hz}$ can therefore not be used.
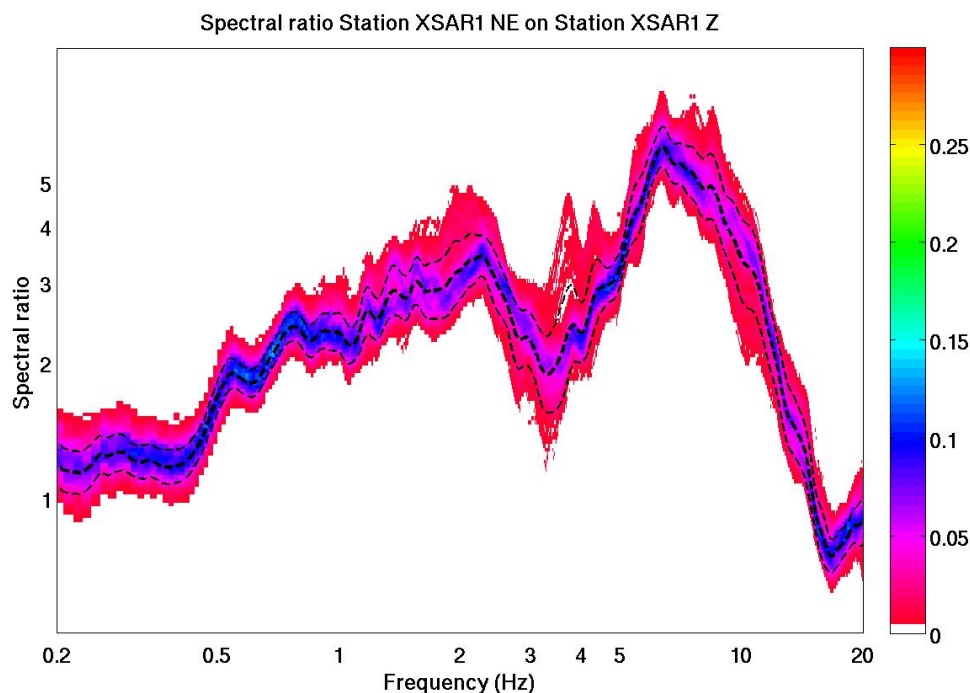
Figure 3: H/V spectral ratios on long recording at station XSAR1, located at the centre of the array.

The fundamental frequency that is found on the long term recording is not always identifiable on the array data due to these disturbances. It can however be retrieved at the value around $2.2\,\text{Hz}$, with lower value in the Southern part. Moreover, Fritsche et al. [2008] did a large amount of H/V measurements in the area Sarnen/Kerns. The interpretation of the H/V peak is not always satisfactory in this study, but it shows fundamental resonance frequencies from approximately $1.1\,\text{Hz}$ in the SE part of the zone of interest, close to the lake, increasing in the edges, with values in our area of interest of $2 - 3\,\text{Hz}$. These data were partly re-interpreted here in order to better understand the context of the station installation (Fig. 5). Even after reinterpretation, some outliers remain, showing how complex H/V interpretation in this area is. From these data, it can be seen that the station is not located on the deepest part of the basin, located in the Southern part and that the layering is highly variable in the basin. The ground motion must also display a high variability in the area.

The H/V curves in the array all show another peak frequency between 5 and $10\,\text{Hz}$, with a value of $7.2\,\text{Hz}$ at the centre. A map of this second peak is displayed on Fig. 6. It shows a strong variability of this resonance with increasing frequency values from W to E.

Moreover, all the methods to compute H/V ratios are compared at the array centre on Fig. 7, in which the classical methods were divided by $\sqrt{2}$ to correct from the Love wave contribution [Fäh et al., 2001]. The classical and TFA methods match all well. The 3C FK analysis (Capon method) does not have resolution down to the peak of the fundamental mode, but provides a similar results. The largest discrepancy comes from the fact that the FK ellipticity does not show the second peak found on the other methods, but a third one just after. The second peak may actually be seen on the 3C analysis but was not picked (Fig. 9).

Figure 4: H/V spectral ratios (time-frequency analysis code V. Poggi).

Figure 5: Map of the fundamental resonance frequencies in Hz, including re-interpreted data from Fritsche et al.
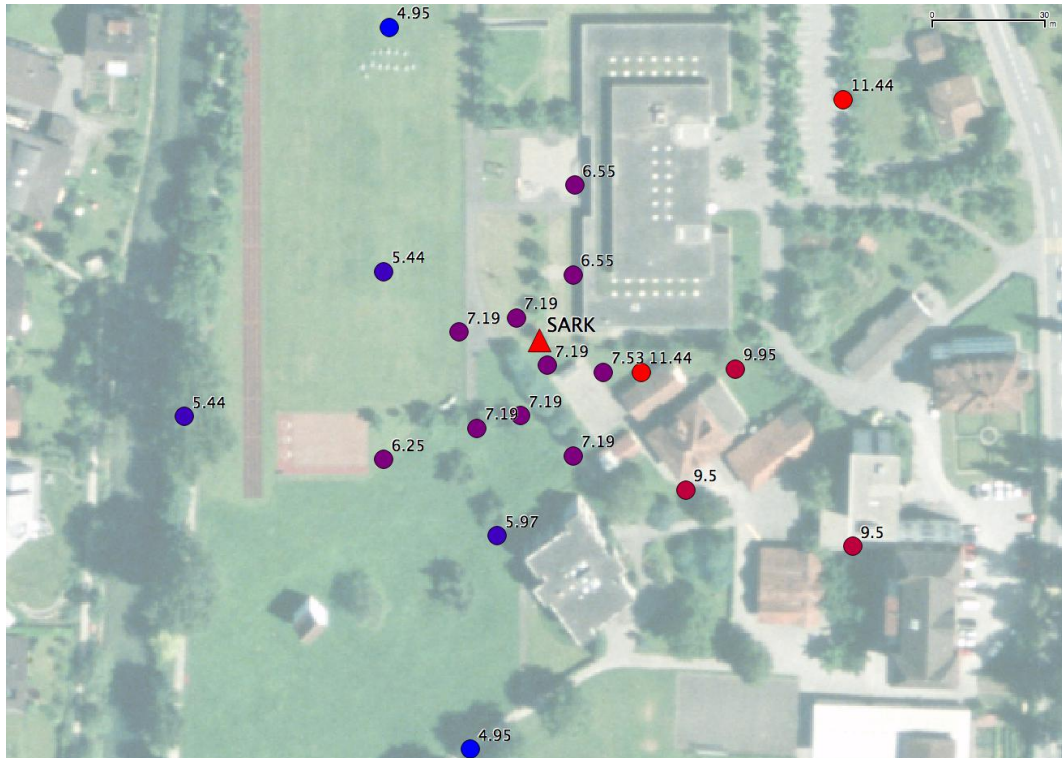[2008].

Figure 6: Map of the second peak in the H/V through the array (frequencies in Hz with redundant color scale.).

In addition, a polarization analysis using the method of Burjánek et al. [2010] was performed but did not show any particular polarization of the ground motion.

The fundamental frequency at the SARK station is therefore at $2.28\,\mathrm{Hz}$, with a low peak amplitude, and a first higher mode is observed around $7\,\mathrm{Hz}$.
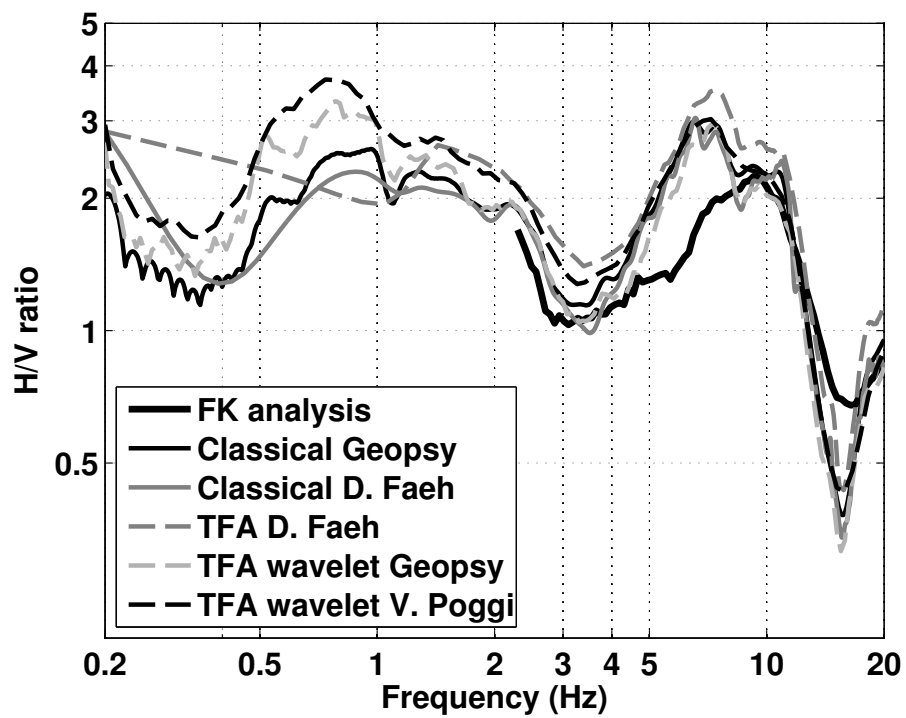
Figure 7: H/V spectral ratios for point SAR000 using the different codes. Classical methods were divided by $\sqrt{2}$.

5 Array processing

5.1 Processing methods and parameters

The vertical components of the arrays were processed using the FK and the High-resolution FK analysis [Capon, 1969] using the Geopsy `http://www.geopsy.org` software. Better results were obtained using large time windows (300T). Each dataset was interpreted separately.

Moreover, a 3C array analysis [Fäh et al., 2008] was also performed using the array_tool_3C software [Poggi and Fäh, 2010]. It allows to derive Rayleigh and Love modes including the Rayleigh ellipticity. Each dataset was interpreted separately.

The array was also processed following the method proposed in Maranò et al. [2012]. Results are obtained jointly modeling up to three propagating plane waves at each time window and frequency. The method models both Rayleigh and Love waves. The recording is split in windows of 20 seconds. Parameter estimation is done via maximum likelihood considering jointly all the measurement from three components sensors. Wavefield parameters estimated include wavenumber, azimuth, and Rayleigh wave ellipticity. Model selection (choice of wave type and number of waves) is performed using the Bayesian information criterion.

Method	Set	Freq. band	Win. length	Anti-trig.	Overlap	Grid step	Grid size	# max.
HRFK 1C	1	$1.5 - 25\,\mathrm{Hz}$	$300T$	No	50%	0.001	0.6	5
HRFK 1C	2	$1.5 - 25\,\mathrm{Hz}$	$300T$	No	50%	0.001	0.6	5
HRFK 3C	1	$2 - 30\,\mathrm{Hz}$	Wav. 10 Tap. 0.2	No	50%	200 m/s	3000 m/s	5
HRFK 3C	2	$2 - 30\,\mathrm{Hz}$	Wav. 10 Tap. 0.2	No	50%	200 m/s	3000 m/s	5
Wavef. dec.	1&2	$1 - 20\,\mathrm{Hz}$	20s					

Table 5: Methods and parameters used for the array processing.

5.2 Obtained dispersion curves

In the vertical component, the interpretation of modes could be done only after comparison of the different methods. Especially the method of Maranò et al. [2012] showed that 2 modes could be seen on dataset 1 and not a single mode (Fig. 10). Using the 1C FK analysis, the first higher mode is picked on the first dataset between 7.5 and 18 Hz (Fig. 8) including its standard deviation. The fundamental mode is picked on the second dataset between 3 and 5.5 Hz (Fig. 8). The velocities are ranging from $1500\,\mathrm{m/s}$ at $3\,\mathrm{Hz}$ down to $1100\,\mathrm{m/s}$ at $5.5\,\mathrm{Hz}$.

Using the 3C analysis, the same two modes (first higher on the first dataset, fundamental on the second dataset) are picked on the vertical component (Fig. 9) and they compare well (Fig. 11). On the radial component, the fundamental Rayleigh mode is also picked on the first dataset and compares well with the method of Maranò et al. [2012] (Fig. 11). On the transverse component, the fundamental Love mode is seen on the first dataset clearly from 8.8 to 20.5 Hz and on the second dataset, less clearly from 2.7 to 5.5 Hz. The first higher Love mode is picked in the first dataset on a short frequency range, but is highly uncertain (Fig. 12).

Finally, using the Maranò et al. [2012] method (Fig. 10), the first dataset gave the best results. The fundamental and first higher Rayleigh modes were picked as well as the fundamental Love mode. For both fundamental Rayleigh and Love, discrepancies are found between the two datasets. It may be due to the fact that this picking is outside the limits of dataset 1. Moreover, there is few energy in this frequency band, increasing the picking uncertainty. Finally it may be due to lateral heterogeneity, though this is not confirmed by the other methods. The ellipticity information could not be retrieve with confidence.

The comparison of the results for Rayleigh curves (Fig. 11) shows that the first higher mode picked from the different methods are consistent. Things are less clear concerning the fundamental mode. Above $7\,\mathrm{Hz}$, i.e. the array limit of the dataset 1, the different methods match. Dataset 2 also provide consistent curves between 2.6 and $5.5\,\mathrm{Hz}$. The inconsistency between the picking in Maranò et al. [2012] method in dataset1 and dataset 2 is assigned to picking issues (and out of limit estimation) and the two parts where the dispersion curve could be accurately picked were joined (Fig. 13). This interpretation is coherent with the inversion (see Section 6). The comparison of the results for Love curves (Fig. 12) displays also a good agreement between 3C FK analysis and the method of Maranò et al. [2012] for the fundamental mode above $8\,\mathrm{Hz}$. At low frequencies, the results are scattered but consistent, the picking from Maranò et al. [2012] method on dataset 2 being discarded. These results are synthesized on Fig. 13.
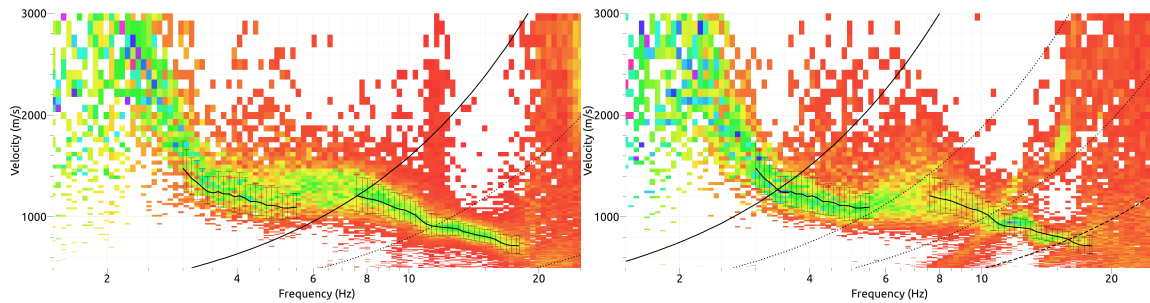

Figure 8: Dispersion curves obtained from the 1C array analysis (left: dataset 1, right: dataset 2).
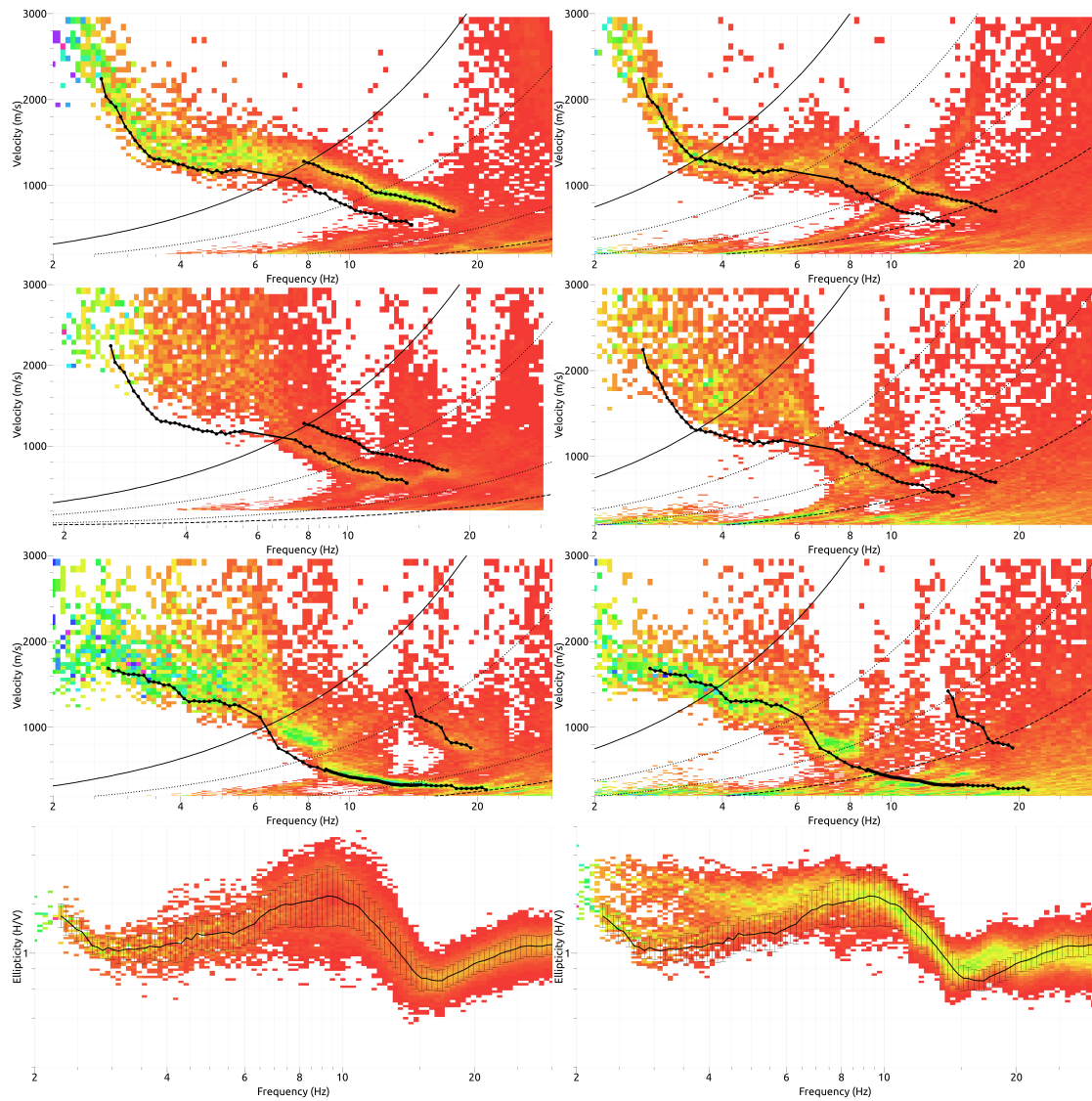
Figure 9: Dispersion curves and ellipticity obtained from the 3C array analysis from the first (left) and second (right) datasets. From top to bottom: vertical, radial and transverse directions and ellipticity.
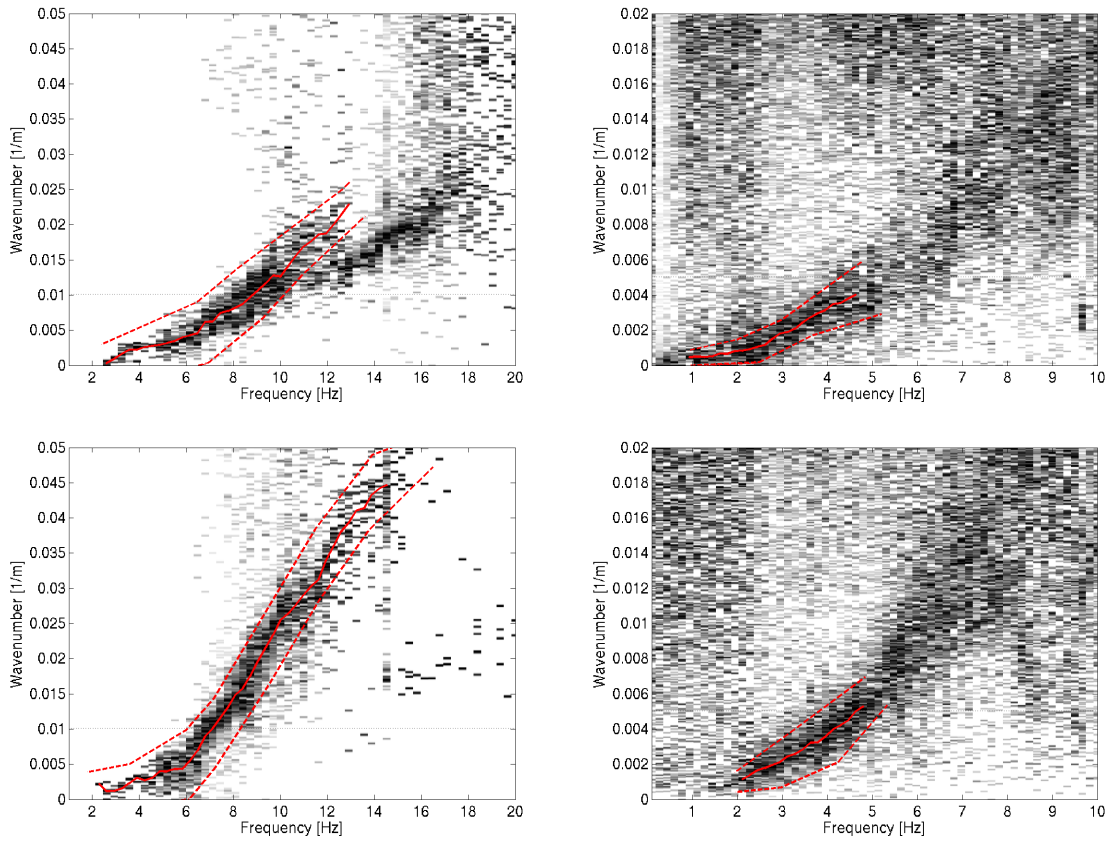
Figure 10: Dispersion picking using the Maranò et al. [2012] method. Top: Rayleigh; Bottom: Love; Left: dataset 1; Right: dataset 2.
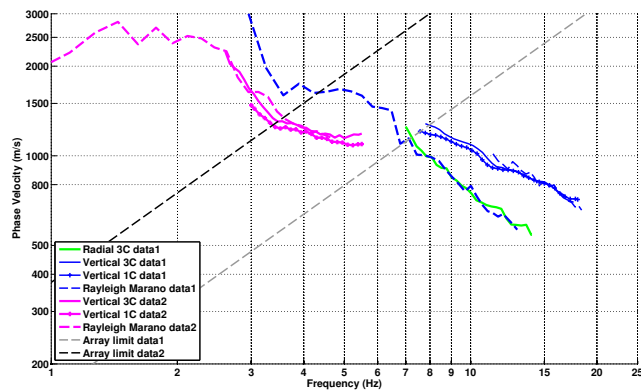

Figure 11: Picked Rayleigh dispersion curves from 1C, 3C FK analyses and Maranò et al. [2012] method for both datasets.
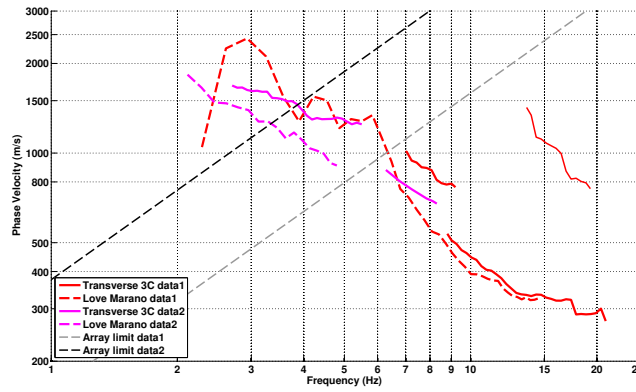
Figure 12: Picked Love dispersion curves from 3C FK analysis and Maranò et al. [2012] method.
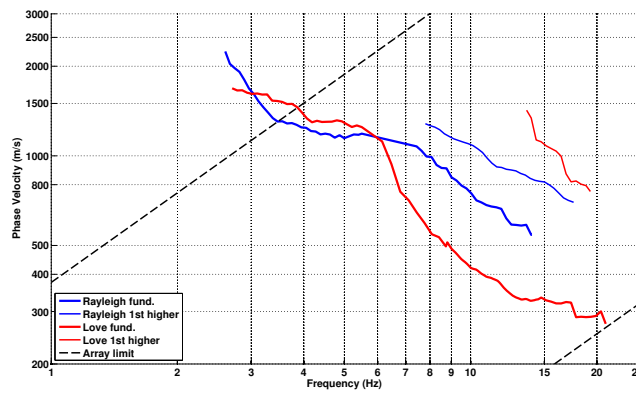

Figure 13: Final interpretation of the dispersion curves.

6   Inversion and interpretation

6.1   Inversion

For the inversion, Rayleigh and Love fundamental and first higher modes dispersion curves, as well as the right flank of ellipticity of the fundamental Rayleigh mode and the ellipticity peak value were used as simultaneous targets, without standard deviation to avoid different weighting. The interpolated part of the dispersion curves were not used. A weight of 0.2 was assigned to the ellipticity information. All curves were resampled using 50 points between 1 and 21 Hz in log scale.

The inversion was performed using the Improved Neighborhood Algorithm (NA) Wathelet [2008] implemented in the Dinver software. In this algorithm, the tuning parameters are the following: Ns_0 is the number of starting models, randomly distributed in the parameter space, Nr is the the number of best cells considered around these Ns_0 models, Ns is the number of new cells generated in the neighborhood of the Nr cells (Ns/Nr per cell) and It_{max} is the number of iteration of this process. The process ends with $Ns_0 + Nr * \frac{Ns}{Nr} * It_{max}$ models. The used parameters are detailed in Tab. 6.

It_{max}	Ns_0	Ns	Nr
500	10000	100	100

Table 6: Tuning parameters of Neighborhood Algorithm.

During the inversion process, low velocity zones were not allowed. The Poisson ratio was inverted in each layer in the range 0.2-0.4, up to 0.47 where the water table is expected. The density was supposed equal to $2000\,\mathrm{kg/m}^3$ except for the deepest layers, assumed to be rock ($2500\,\mathrm{kg/m}^3$). Inversions with free layer depths as well as fixed layer depths were performed. 4 layers are enough to explain most of the targets (dispersion and ellipticity), but more layers are used to smooth the obtained results and better explore the parameter space. 5 independent runs of 5 different parametrization schemes (5 and 6 layers over a half space and 10, 12 and 14 layers with fixed depth) were performed. For further elaborations, the best models of these 25 runs were selected (Fig. 17).

A first layer of approximately $8\,\mathrm{m}$ is found with a low velocity around $270\,\mathrm{m/s}$ (Fig. 14 and Fig. 17). At this depth a clear interface is found, with velocities in the lower part starting around $800\,\mathrm{m/s}$ at $10\,\mathrm{m}$ and increasing linearly to $1400\,\mathrm{m/s}$ at $40\,\mathrm{m}$. At this depth, no more velocity change is found down to the bedrock, found around $160\,\mathrm{m}$. This may indicate the presence of a velocity inversion but no data can constrain it. The velocity in the bedrock may be large, but the data do not really constrain it. Finally, even if the ellipticity gives some constrain on the bedrock depth, it is still largely unknown.

When comparing to the target curves (Fig. 15 and Fig. 16), all curves are correctly represented.
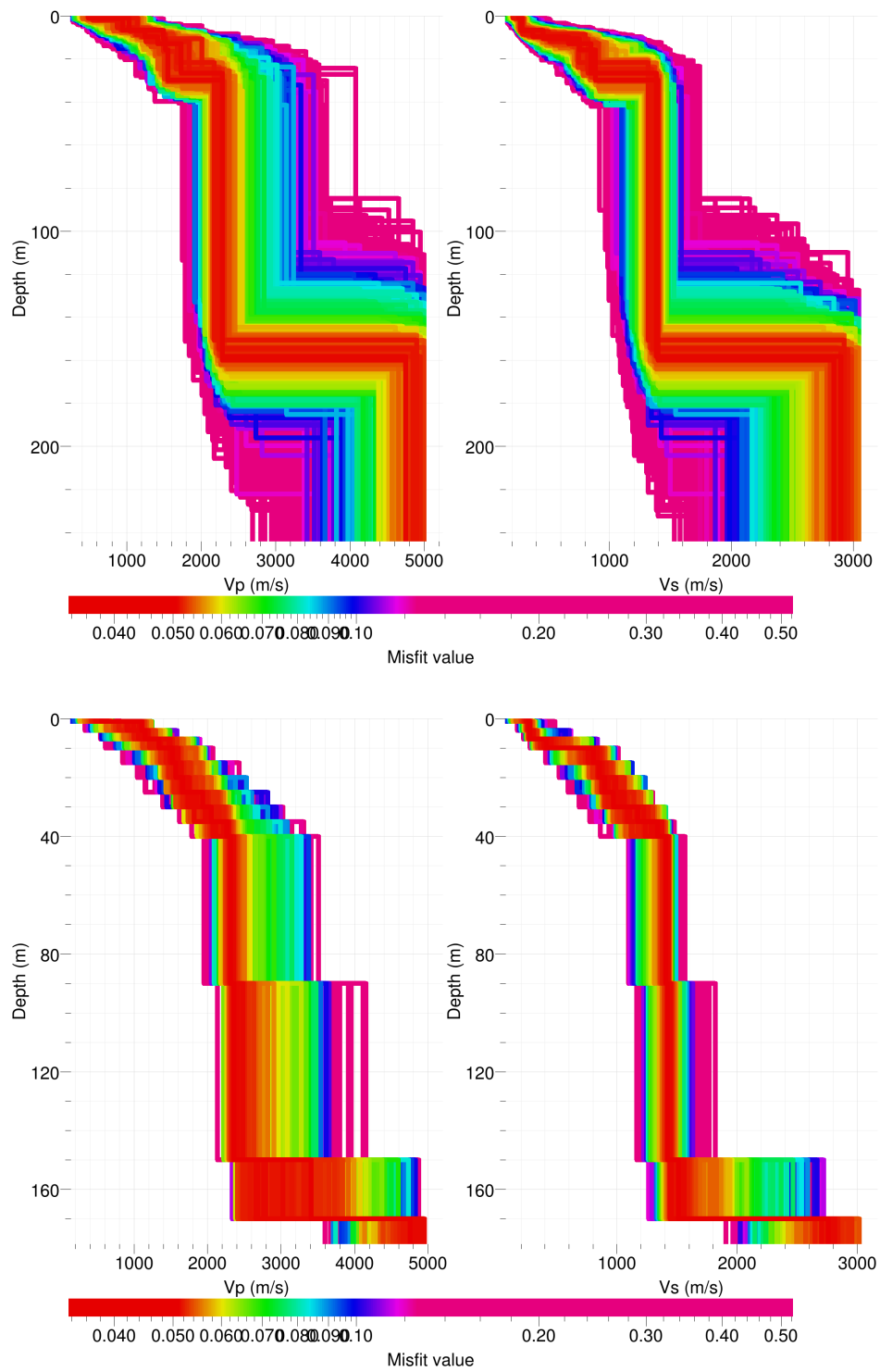
Figure 14: Inverted ground profiles in terms of V_p and V_s; top: free layer depth strategy; bottom: fixed layer depth strategy.
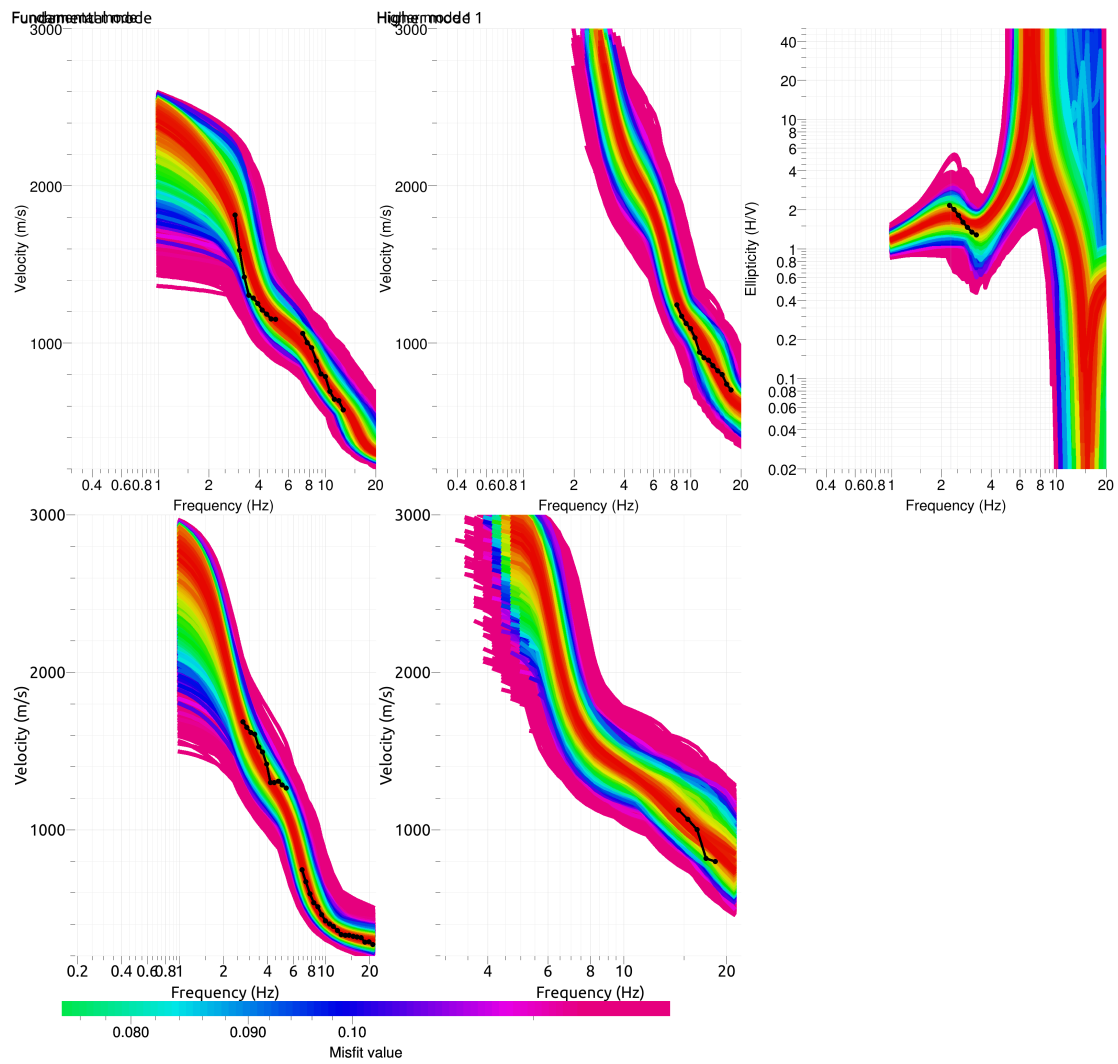
Figure 15: Comparison between inverted models and measured Rayleigh and Love modes and corresponding ellipticity, free layer depth strategy.
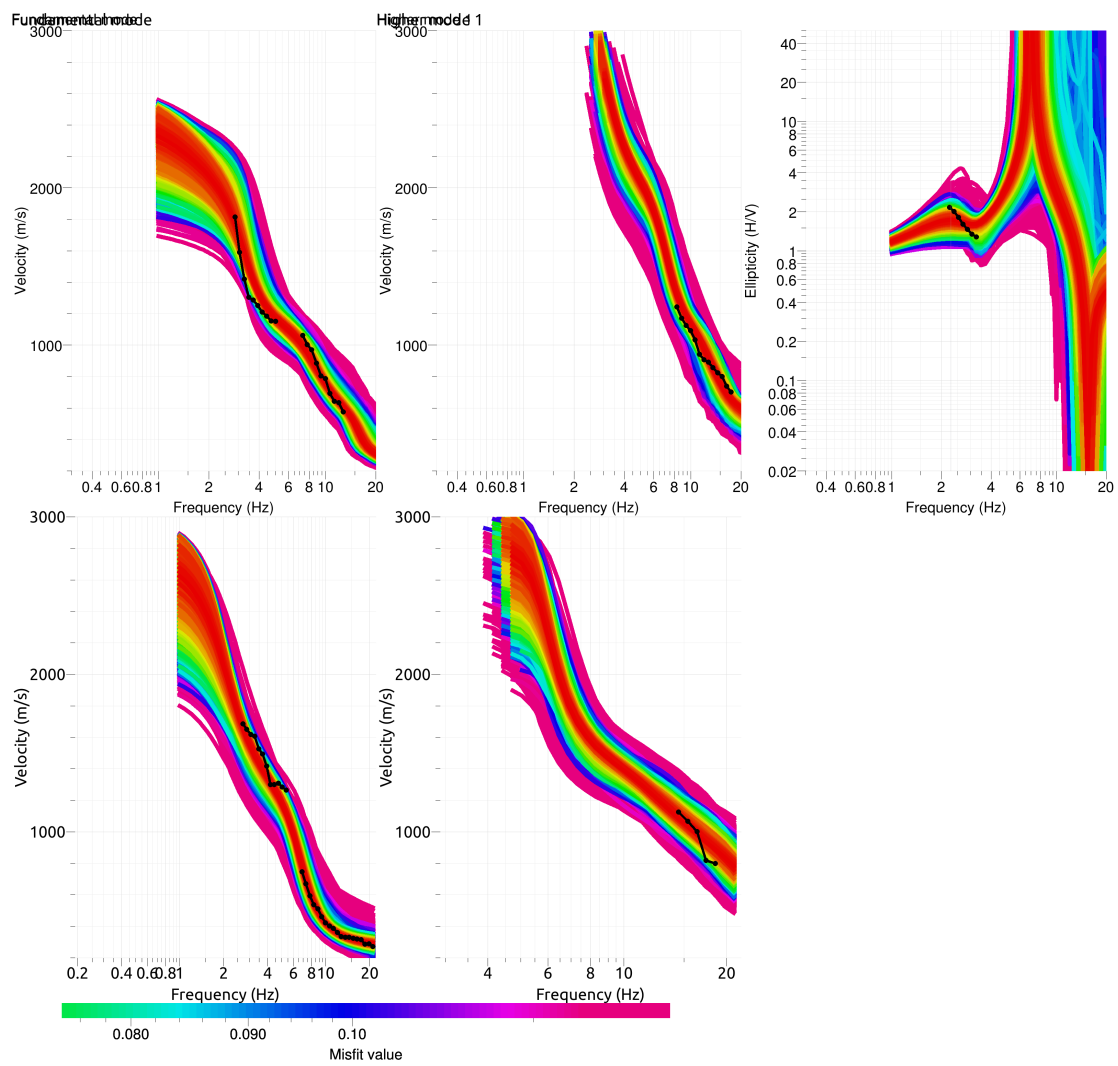
Figure 16: Comparison between inverted models and measured Rayleigh and Love modes and corresponding ellipticity, fixed layer depth strategy.
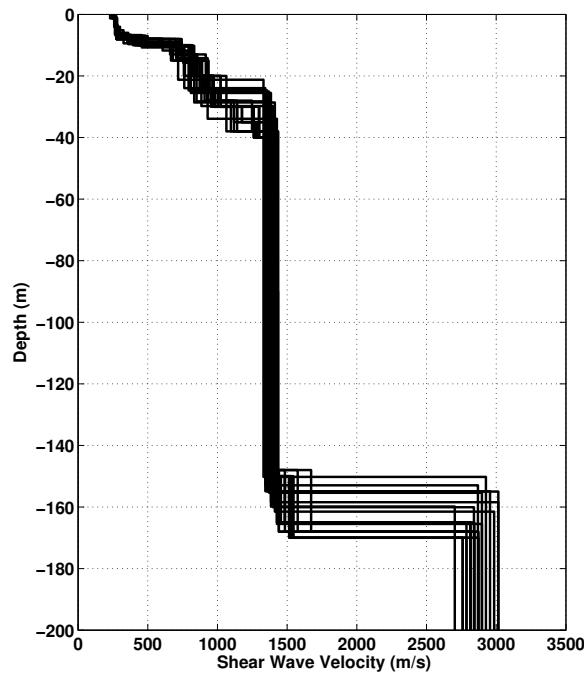
Figure 17: V_s ground profiles for the selected 25 best models.

The results are compared to station SARG, located in to the North. The SARG analysis was performed by Steiner (2004) in its Master thesis but the original data could not be found for quality check. The H/V analysis of the two sites show similar features (Fig. 18), though shifted to higher frequencies at SARG with a fundamental peak at 2.9 and $2.3\,\mathrm{Hz}$, for SARG and SARK, respectively. The dispersion curves confirm the shift to higher frequencies in SARG but show quite different curves. The velocity profiles (Fig. 20) at both sites are compared. However, these two series of profiles are relatively similar. At SARG, a velocity inversion is proposed between 40 and $70\,\mathrm{m}$ but is hardly constrain by the data. As explained, such an inversion is possible at SARK even though it would be hardly constrained by the data. Moreover, the bedrock is not found in the SARG inversion. In the SARK inversion, this interface is producing the first peak in the fundamental resonance. As a conclusion, sites SARK and SARG show similarities, although located at both ends of the city of Sarnen.
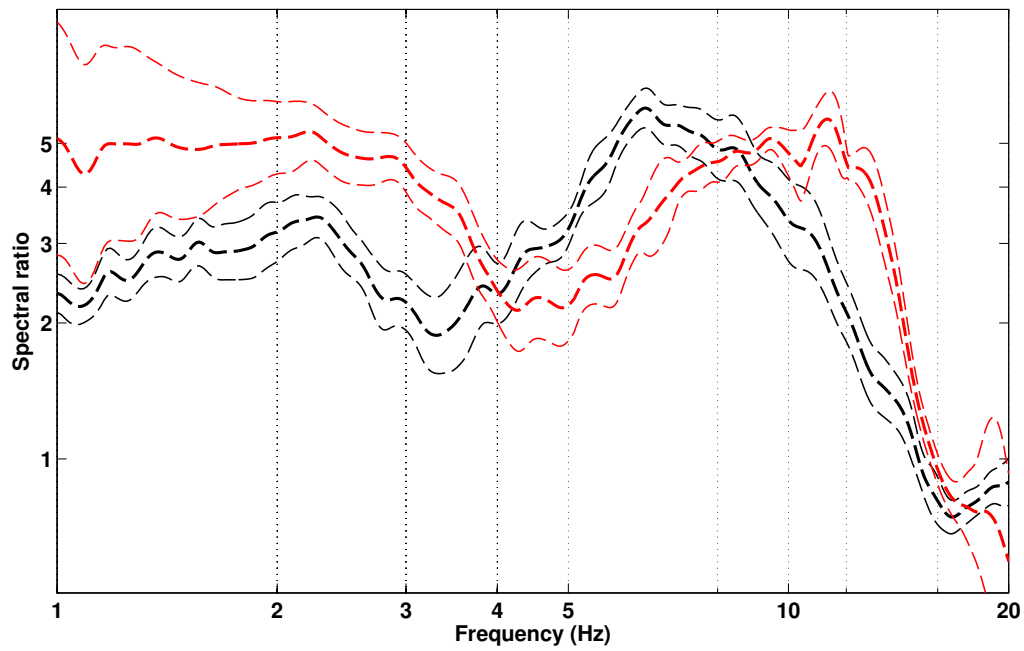
Figure 18: Comparison of H/V curves for station SARK (black) compared to station SARG (red).
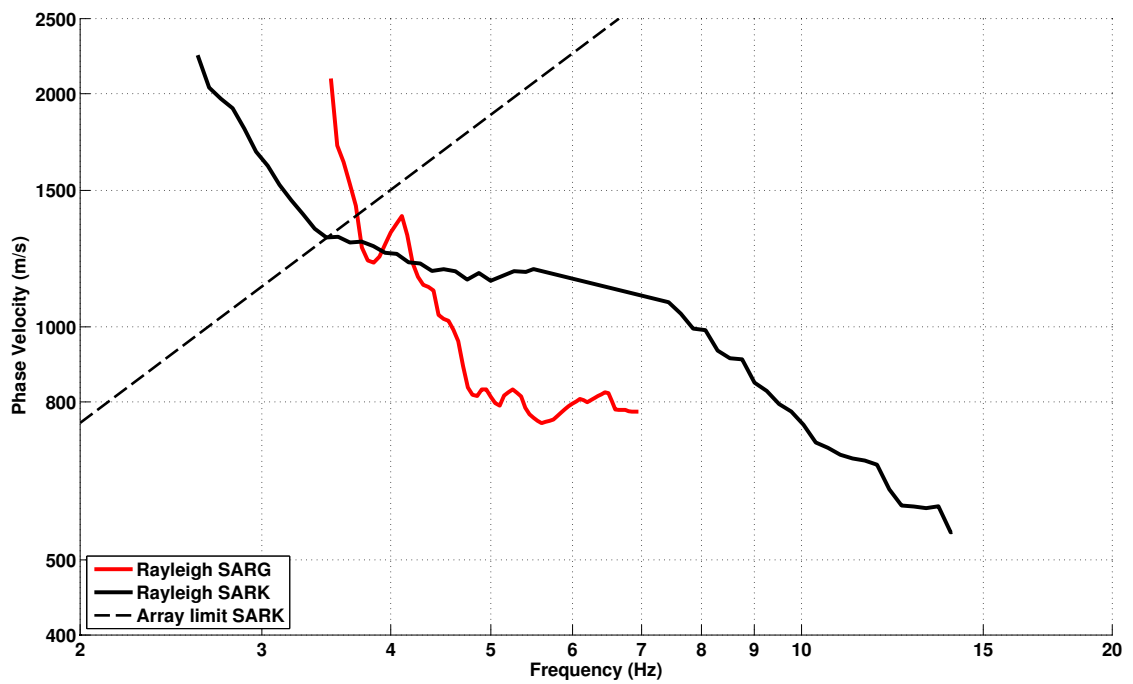

Figure 19: Comparison of Rayleigh dispersion curves for station SARK (black) compared to station SARG (red).
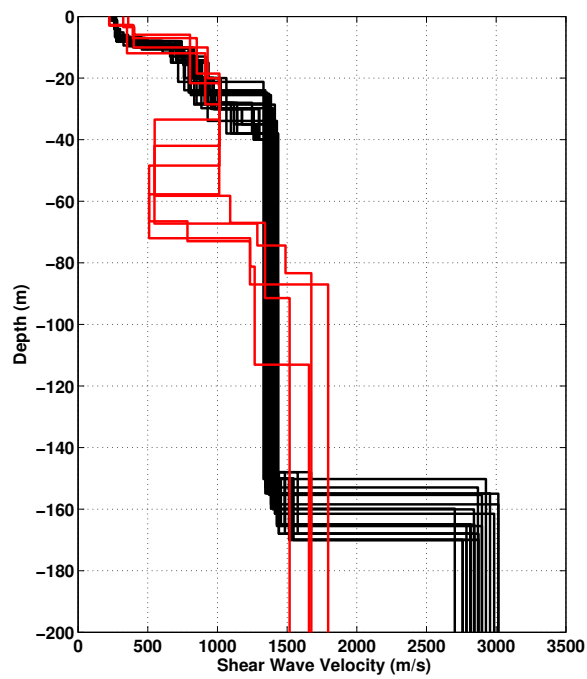
Figure 20: V_s ground profiles for station SARK (black) compared to profiles for station SARG (red).

6.2 Travel time average velocities and ground type

The distribution of the travel time average velocities at different depths was computed from the selected models. The uncertainty, computed as the standard deviation of the distribution of travel time average velocities for the considered models, is also provided, but its meaning is doubtful. $V_{s,30}$ is found to be $540\,\mathrm{m/s}$. Considering the first weak layer ($8 - 10\,\mathrm{m}$) on top on hard sediments, the site can be classified as class E, in the Eurocode 8 [CEN, 2004] and in SIA261 [SIA, 2003].

	Mean (m/s)	Uncertainty (m/s)
$V_{s,5}$	268	4
$V_{s,10}$	307	4
$V_{s,20}$	442	5
$V_{s,30}$	541	5
$V_{s,40}$	632	5
$V_{s,50}$	709	5
$V_{s,100}$	939	6
$V_{s,150}$	1055	10
$V_{s,200}$	-	-

Table 7: Travel time averages at different depths from the inverted models. Uncertainty is given as one standard deviation from the selected profiles.

6.3 SH transfer function and quarter-wavelength velocity

The quarter-wavelength velocity approach [Joyner et al., 1981] provides, for a given frequency, the average velocity at a depth corresponding to 1/4 of the wavelength of interest. It is useful to identify the frequency limits of the experimental data (minimum frequency in ellipticity, $2.3\,\mathrm{Hz}$ here, and dispersion curves, $2.7\,\mathrm{Hz}$ here). The results using this proxy show that no data is controlling the results below $105\,\mathrm{m}$, and the dispersion curves are controlling the results down to $80\,\mathrm{m}$ (Fig. 21). Moreover, the quarter wavelength impedance-contrast introduced by Poggi et al. [2012a] is also displayed in the figure. It corresponds to the ratio between two quarter-wavelength average velocities, respectively from the top and the bottom part of the velocity profile, at a given frequency [Poggi et al., 2012a]. It shows a trough (inverse shows a peak) at the resonance frequency.

Moreover, the theoretical SH-wave transfer function for vertical propagation [Roesset, 1970] is computed from the inverted profiles. It is compared to the quarter-wavelength amplification [Joyner et al., 1981], that however cannot take resonances into account (Fig. 22). In this case, the models are predicting an amplification up to a factor of 7 at the second peak of the resonance around $6 - 8\,\mathrm{Hz}$, but lower amplification (around 2) at the fundamental frequency at $2.3\,\mathrm{Hz}$. However, anelastic attenuation may strongly decrease this high frequency elastic amplification. This will be compared to observations at this station.
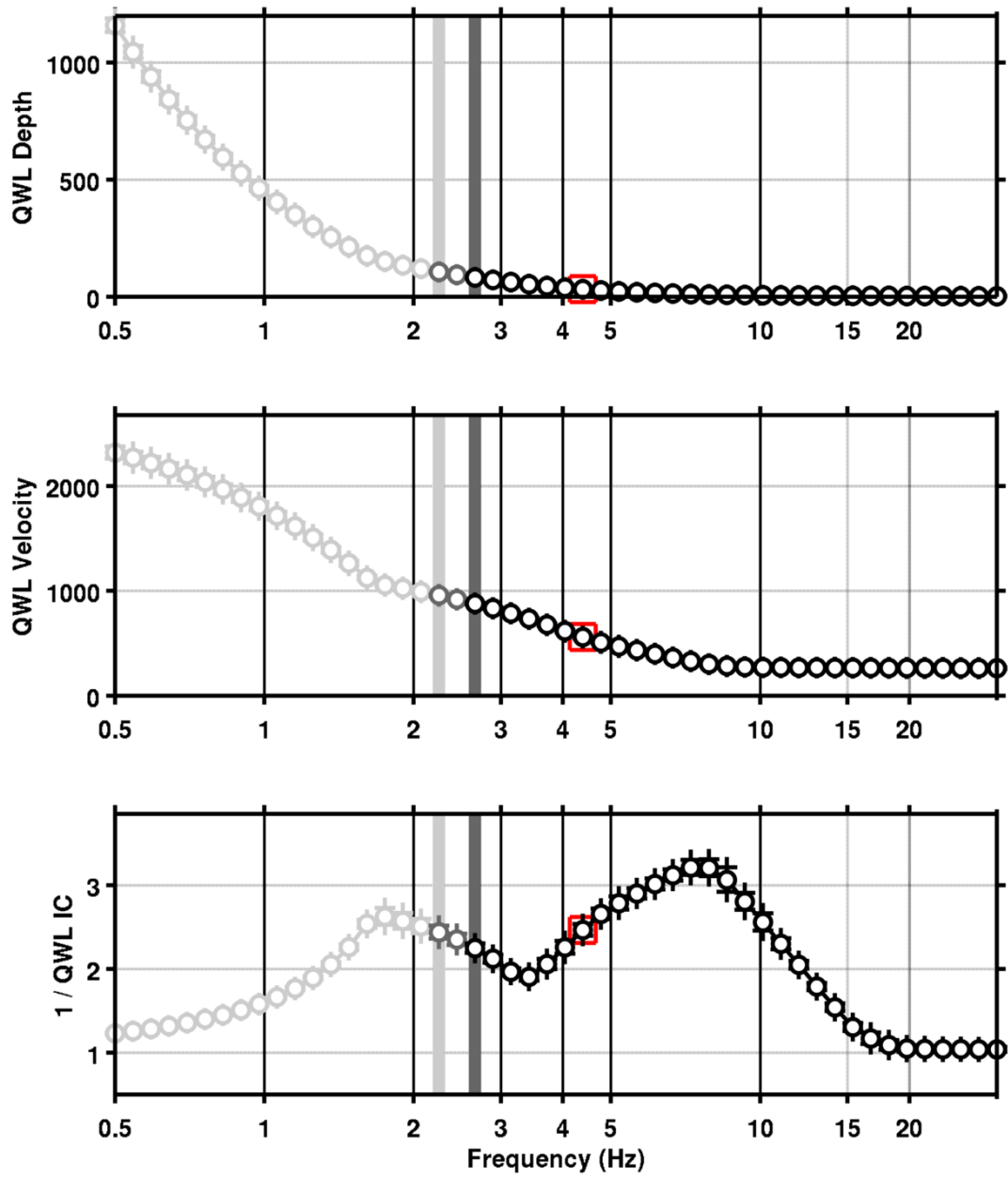
Figure 21: Quarter wavelength velocity representation of the velocity profile (top: depth, centre: velocity, bottom: inverse of the impedance contrast). Black curve is constrained by the dispersion curves, light grey is not constrained by the data. Red square is corresponding to $V_{s,30}$.
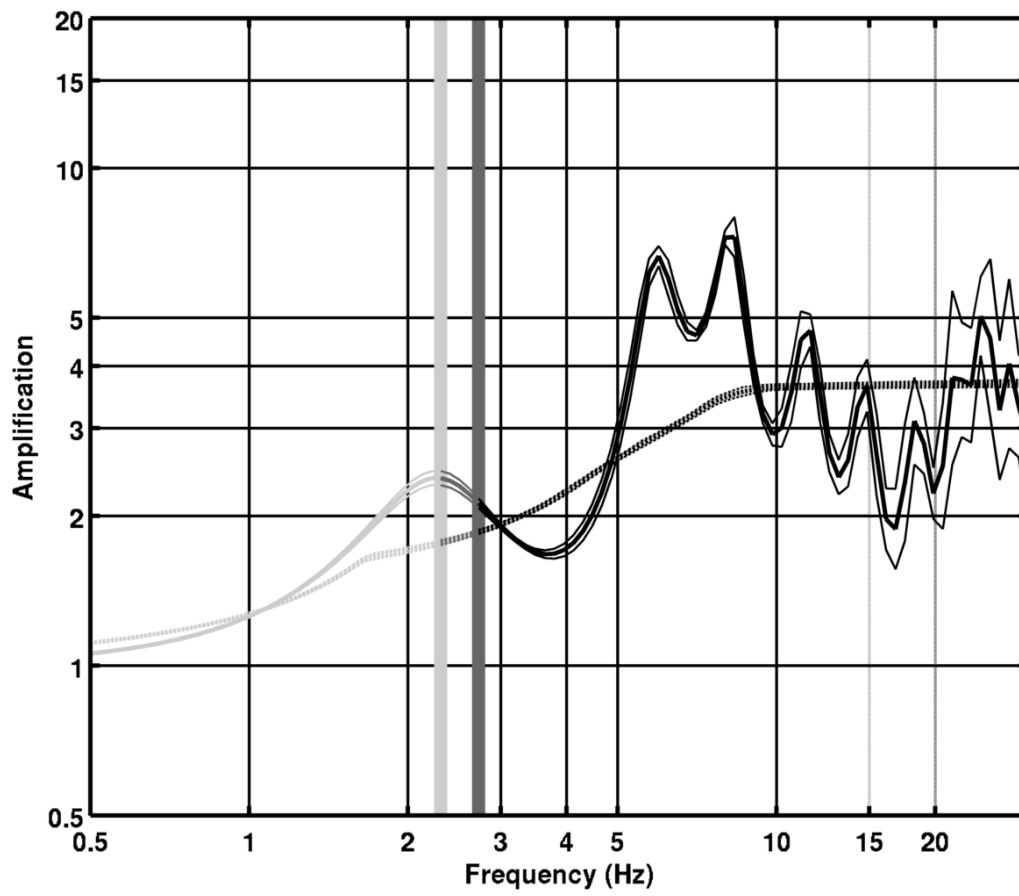
Figure 22: Theoretical SH transfer function (solid line) and quarter wavelength impedance contrast (dashed line) with their standard deviation. Significance of the greyshades is detailed in Fig. 21.

7   Conclusions

The array measurements performed in this study were successful in deriving a velocity model below the SARK station. We found a $8 - 10\,\mathrm{m}$ sedimentary layer with $V_s = 270\,\mathrm{m/s}$ on more consolidated sediments with a velocity larger than $V_s = 800\,\mathrm{m/s}$. The velocity reaches $1400\,\mathrm{m/s}$ at $40\,\mathrm{m}$ and is stable down to the bedrock, found around $160\,\mathrm{m}$ with a large uncertainty. This velocity contrast produces a fundamental resonance peak at $2.3\,\mathrm{Hz}$. Contrarily to what was expected, the infill sediments of this basin are very stiff except the very upper part. $V_{s,30}$ is found to be close to $540\,\mathrm{m/s}$. For the design codes, this configuration corresponds to ground type E. The theoretical SH transfer function and impedance contrast of the quarter-wavelength velocity computed from the inverted profiles show a large amplification around at $6 - 8\,\mathrm{Hz}$. Recordings on the new station will allow to validate these simple models.

Acknowledgements

References

Sylvette Bonnefoy-Claudet, Fabrice Cotton, and Pierre-Yves Bard. The nature of noise wavefield and its applications for site effects studies. *Earth-Science Reviews*, 79(3-4): 205–227, December 2006. ISSN 00128252. doi: 10.1016/j.earscirev.2006.07.004. URL http://linkinghub.elsevier.com/retrieve/pii/S0012825206001012.

Jan Burjánek, Gabriela Gassner-Stamm, Valerio Poggi, Jeffrey R. Moore, and Donat Fäh. Ambient vibration analysis of an unstable mountain slope. *Geophysical Journal International*, 180(2):820–828, February 2010. ISSN 0956540X. doi: 10.1111/j.1365-246X.2009.04451.x. URL http://doi.wiley.com/10.1111/j.1365-246X.2009.04451.x.

J. Capon. High-Resolution Frequency-Wavenumber Spectrum Analysis. *Proceedings of the IEEE*, 57(8):1408–1418, 1969.

CEN. *Eurocode 8: Design of structures for earthquake resistance - Part 1: General rules, seismic actions and rules for buildings*. European Committee for Standardization, en 1998-1: edition, 2004.

Donat Fäh, Fortunat Kind, and Domenico Giardini. A theoretical investigation of average H / V ratios. *Geophysical Journal International*, 145:535–549, 2001.

Donat Fäh, Gabriela Stamm, and Hans-Balder Havenith. Analysis of three-component ambient vibration array measurements. *Geophysical Journal International*, 172(1):199–213, January 2008. ISSN 0956540X. doi: 10.1111/j.1365-246X.2007.03625.x. URL http://doi.wiley.com/10.1111/j.1365-246X.2007.03625.x.

Donat Fäh, Marc Wathelet, Miriam Kristekova, Hans-Balder Havenith, Brigitte Endrun, Gabriela Stamm, Valerio Poggi, Jan Burjanek, and Cécile Cornou. Using Ellipticity Information for Site Characterisation Using Ellipticity Information for Site Characterisation. Technical report, NERIES JRA4 Task B2, 2009.

Stefan Fritsche, Donat Fäh, Brian Steiner, and Domenico Giardini. Damage field and site effects: multidisciplinary studies of the 1964 earthquake series in Central Switzerland. *Natural Hazards*, 48(2):203–227, July 2008. ISSN 0921-030X. doi: 10.1007/s11069-008-9258-y. URL http://www.springerlink.com/index/10.1007/s11069-008-9258-y.

William B. Joyner, Richard E. Warrick, and Thomas E. Fumal. The effect of Quaternary alluvium on strong ground motion in the Coyote Lake, California, earthquake of 1979. *Bulletin of the Seismological Society of America*, 71(4):1333–1349, 1981.

Katsuaki Konno and Tatsuo Ohmachi. Ground-Motion Characteristics Estimated from Spectral Ratio between Horizontal and Vertical Components of Microtremor. *Bulletin of the Seismological Society of America*, 88(1):228–241, 1998.

Stefano Maranò, C. Reller, H.-A. Loeliger, and Donat Fäh. Seismic waves estimation and wave field decomposition: Application to ambient vibrations. *Geophysical Journal International*, submitted, 2012.

Valerio Poggi and Donat Fäh. Estimating Rayleigh wave particle motion from three-component array analysis of ambient vibrations. *Geophysical Journal International*, 180(1):251–267, January 2010. ISSN 0956540X. doi: 10.1111/j.1365-246X.2009.04402.x. URL `http://doi.wiley.com/10.1111/j.1365-246X.2009.04402.x`.

Valerio Poggi, Benjamin Edwards, and D. Fah. Characterizing the Vertical-to-Horizontal Ratio of Ground Motion at Soft-Sediment Sites. *Bulletin of the Seismological Society of America*, 102(6):2741–2756, December 2012a. ISSN 0037-1106. doi: 10.1785/0120120039. URL `http://www.bssaonline.org/cgi/doi/10.1785/0120120039`.

Valerio Poggi, Donat Fäh, Jan Burjanek, and Domenico Giardini. The use of Rayleigh-wave ellipticity for site-specific hazard assessment and microzonation: application to the city of Lucerne, Switzerland. *Geophysical Journal International*, 188(3):1154–1172, March 2012b. ISSN 0956540X. doi: 10.1111/j.1365-246X.2011.05305.x. URL `http://doi.wiley.com/10.1111/j.1365-246X.2011.05305.x`.

J.M. Roesset. Fundamentals of soil amplification. In R. J. Hansen, editor, *Seismic Design for Nuclear Power Plants*, pages 183–244. M.I.T. Press, Cambridge, Mass., 1970. ISBN 978-0-262-08041-5. URL `http://mitpress.mit.edu/catalog/item/default.asp?ttype=2\&tid=5998`.

SIA. *SIA 261 Actions sur les structures porteuses*. Société suisse des ingénieurs et des architectes, Zürich, sia 261:20 edition, 2003.

Marc Wathelet. An improved neighborhood algorithm: Parameter conditions and dynamic scaling. *Geophysical Research Letters*, 35(9):1–5, May 2008. ISSN 0094-8276. doi: 10.1029/2008GL033256. URL `http://www.agu.org/pubs/crossref/2008/2008GL033256.shtml`.